

Adjoint-Assisted Topology-Optimization-Inspired Analysis of Pseudo-Porous Flow Fields: Application to a Flettner Rotor

Niklas Kühl*¹

¹Hamburg Ship Model Basin, Bramfelder Strasse 164, D-22305 Hamburg, Germany

May 9, 2025

Abstract

This paper presents an adjoint-assisted, topology-optimization-inspired approach for analyzing topological sensitivities in fluid domains based on porous media formulations – without directly utilizing the porosity field as a design variable. Instead, the method evaluates the sensitivity with respect to the porosity parameter via an indirect, adjoint formulation, enabling intuitive visualization of cost-functional improving or deteriorating regions. These sensitivity fields are not used in a classical optimization loop but rather to qualitatively assess spatial areas that indicate potential for flow improvement. A key benefit of the proposed approach is its non-intrusive nature: no modifications to existing adjoint solvers, e.g., for shape optimization purposes, are required. As such, the method can be interpreted as an alternative post-processing step that supports early-stage design insights. The approach is demonstrated on a Flettner rotor operating in atmospheric wind at a diameter-based Reynolds number and spinning ratio of $Re_D = 2 \cdot 10^6$ as well as $k = 3$ to highlight its practical relevance and interpretability. Placing a container stack in cost-functional improving or deteriorating areas validates the method’s prediction quality of topological flow sensitivities.

Keywords: Computational Fluid Dynamics, Modeling, Simulation & Optimization, Continuous Adjoint Sensitivity Analysis, Topology Optimization, Flettner Rotor, Maritime Aerodynamics

1 Introduction

Design optimization in Computational Fluid Dynamics (CFD), particularly shape and topology optimization, is critical in enhancing performance across various engineering applications, cf. Papoutsis-Kiachagias and Giannakoglou (2016); Bendsoe and Sigmund (2013). Among the established methodologies, topology optimization based on porous media formulations has proven effective for identifying optimal material distributions in flow domains (Sigmund and Maute (2013); Bendsoe and Sigmund (2013)). These methods mostly rely on parameterized porosity fields and gradient-based algorithms to iteratively evolve domain topology toward improved flow performance, e.g. Gerdes et al. (2014); Vrionis et al. (2021).

Initial applications of fluid mechanical topology optimization, in particular, addressed creeping flows, cf. Borrvall and Petersson (2003); Guest and Prévost (2006). Since then, the method’s complexity has increased remarkably and has been widely applied, e.g., to ducted scenarios (Gersborg-Hansen et al. (2005); Othmer (2008)) as well as flows including heat transfer (Ruberto (2016); Pizzolato et al. (2017, 2019)). In addition to phase field methods (Blank et al. (2012); Garcke et al. (2015)), formulations based on Darcy or Forchheim porosities (Guest and Prévost (2006); Othmer et al. (2017)) have been established. Typical discretization schemes follow weighted residual approaches, e.g., Finite-Element/Volume-Methods (Olesen et al. (2006); Garcke et al. (2015); Gerdes et al. (2014); Papoutsis-Kiachagias and Giannakoglou (2016)), or apply kinetic CFD (Nørgaard et al. (2016); Klemens et al. (2020)) approaches.

Despite their theoretical appeal, classical topology optimization approaches require solid modifications to existing flow solvers, especially when adjoint-based gradient information must be computed and incorporated into an optimization loop, cf. Yu et al. (2011); Xu et al. (2014). This presents practical challenges, particularly when working with complex or proprietary solvers or when design exploration is preferred over strict optimality, which is usually the case in the initial design stage.

This work presents a topology-optimization-inspired, adjoint-assisted method that bypasses these limitations. Rather than embedding porosity into the primal flow field, sensitivities are computed with respect to a virtual

*kuehl@hsva.de

porosity parameter via an adjoint framework—without ever altering the physical model – and thus, the CFD solver. The resulting sensitivity fields can be visually interpreted by simply checking the sign to identify regions with potentials flow improvement. Importantly, the approach is purely diagnostic and non-intrusive: it acts as a post-processing step and does not require solver modifications or optimization infrastructure.

This paper utilizes the continuous adjoint method (Giles and Pierce (1997, 2000); Othmer (2008)), although the idea can be followed via the discrete-adjoint route (Nadarajah (2003); Roth and Ulbrich (2013); Gauger et al. (2008)). To demonstrate the utility and interpretability of this approach, a canonical Flettner rotor configuration is investigated, cf. Seifert (2012).

The structure of the manuscript is as follows. The upcoming Sec. 2 provides an overview of the basic model equations and their discrete approximation. Subsequently, Sec. 3 applies the presented method to the analysis of an isolated Flettner rotor in an idealized wind tunnel under atmospheric wind at a diameter-based Reynolds number and spinning ratio of $\text{Re}_D = 2 \cdot 10^6$ as well as $k = 3$. The proposed method is validated by placing a container stack in cost-functional improving or deteriorating regions via re-evaluating objectives on the new designs. The manuscript ends with a summary and outlook in Sec. 4. The paper defines vectors and tensors concerning a fixed orthogonal coordinate system, applying Einstein’s summation convention to doubly occurring Latin indices.

2 Mathematical Model

The paper’s work utilizes a hybrid averaged/filtered turbulent flow simulation framework that mixes elements of Unsteady Reynolds-Averaged Navier-Stokes (URANS) and Large-Eddy Simulation (LES) strategies in line with the Detached-Eddy Simulation (DES) approach. The following baseline set of equations refers to the local balance of mass and linear momentum and governs the temporal (t) evolution of an incompressible fluid’s (ρ , μ) velocity v_i and pressure p , viz.

$$-\frac{\partial v_k}{\partial x_k} = 0, \quad (1)$$

$$\frac{\partial \rho v_i}{\partial t} + \frac{\partial v_k \rho v_i}{\partial x_k} + \frac{\partial}{\partial x_k} [p^{\text{eff}} \delta_{ik} - 2\mu^{\text{eff}} S_{ik}] + \alpha (v_i - v_i^{\text{tar}}) = 0, \quad (2)$$

where $S_{ik} = 1/2(\partial v_i/\partial x_k + \partial v_k/\partial x_i)$ represents the strain rate tensor, $p^{\text{eff}} = p + p^t$ as well as $\mu^{\text{eff}} = \mu + \mu^t$ denote effective pressure and viscosity, respectively, and $\alpha \geq 0$ of unit $\text{kg}/(\text{sm}^3)$ describes a penalty quantity that drives the fluid velocity vector towards a prescribed target value v_i^{tar} . The approach is frequently applied during the discrete treatment in flow solvers when a specific solution is to be enforced or fades out, e.g., in the case of sea state boundary conditions, cf. Woekner et al. (2010); Loft et al. (2023). Commonly, the target flow velocity vanishes $v_i^{\text{tar}} \rightarrow 0$ in line with Darcy’s law acting as a momentum sink in the corresponding balance equation. Throughout the paper, the penalty or Darcy parameter is constantly zero and refers to an imaginary quantity that serves as a control measure to indicate topological sensitivities. Alternatives based on a Forchheimer formulation are also conceivable, but these are not discussed in this paper. Turbulent quantities in Eqns. (2) follow the Improved Delayed DES model of Gritskevich et al. (2012). Further model details are provided in the appendices of Kühl et al. (2024) or Kühl (2025a). The following boundary conditions are used for considering Flettner-rotor performances in an idealized numerical wind-tunnel along inner walled (Γ^{wall}) and lower symmetry (Γ^{symm}) as well as horizontal (Γ^{hor}) and upper (Γ^{top}) far field boundaries:

$$\frac{\partial p}{\partial n} = 0, v_i = V_i^{\text{wall}} \quad \text{on} \quad \Gamma^{\text{wall}}, \quad (3)$$

$$\frac{\partial p}{\partial n} = 0, v_i = V_i^{\text{hor}} \quad \text{on} \quad \Gamma^{\text{hor}}, \quad (4)$$

$$\frac{\partial p}{\partial n} = 0, \frac{\partial v_i}{\partial n} = 0 \quad \text{on} \quad \Gamma^{\text{symm}}, \quad (5)$$

$$p = P, \frac{\partial v_i}{\partial n} = 0 \quad \text{on} \quad \Gamma^{\text{top}}. \quad (6)$$

Therein, P denotes a reference pressure and $V_i^{\text{hor}} = V_{\text{ref}}(x_3/x_{3,\text{ref}})^m \delta_{i1}$ follows an atmospheric wind profile that points in x_1 and develops in x_3 direction, respectively. A Flettner rotor’s rotational velocity follows $V_i^{\text{wall}} = (\pi D f) t_i$ based on the rotor Diameter D , the rotational frequency f , and the circumferential vector t_i . Initial conditions extend the atmospheric profile into the interior, i.e., $p(x_i, t = 0) = P$ and $v_i(x_i, t) = V_i^{\text{hor}}$.

This paper aims to determine topological sensitivities of the time-averaged, statistically converged flow field to identify regions in the vicinity of a Flettner rotor to judge on the influence of material placement on the

performance of the rotor. All forward calculations are carried out until the averaged flow fields are converged, which motivates the following cost function

$$J = \frac{1}{t_{\text{end}} - t_{\text{start}}} \int_{t_{\text{start}}}^{t_{\text{end}}} \int [p^{\text{eff}} \delta_{ik} - 2\mu^{\text{eff}} S_{ik}] n_k r_i d\Gamma^{\text{O}} dt \quad \rightarrow \quad J = \int [\bar{p}^{\text{eff}} \delta_{ik} - 2\bar{\mu}^{\text{eff}} \bar{S}_{ik}] n_k r_i d\Gamma^{\text{O}} \quad (7)$$

where overlined quantities are no longer a function of time due to averaging, i.e., $\bar{v}_i := \bar{v}_i(x_i)$ and $\bar{p} := \bar{p}(x_i)$, and n_k as well as r_i describe the local surface normal vector and the direction of the force under consideration, e.g., drag or lift. The cost functional is restricted to certain boundaries of the fluid domain ($\Gamma^{\text{O}} \subset \Gamma^{\text{wall}} \subset \Gamma$), i.e., the Flettner rotor.

In line with the temporally constant cost functional, the following augmented cost functional a.k.a. Lagrangian is constructed by adding the time averaged flow equations (cf. Eqns. (1) and (2)), i.e.,

$$L = J + \int \hat{v}_i \left[\frac{\partial}{\partial x_k} [\bar{v}_k \rho \bar{v}_i + \bar{p}^{\text{eff}} \delta_{ik} - 2\bar{\mu}^{\text{eff}} \bar{S}_{ik}] + \alpha (\bar{v}_i - v_i^{\text{tar}}) \right] - \hat{p} \frac{\partial \bar{v}_k}{\partial x_k} d\Omega, \quad (8)$$

which introduces the adjoint velocity \hat{v}_i and pressure \hat{p} in terms of Lagrangian multipliers. Dimensions of the adjoint variables follow the objective functional and read $[\hat{v}_i] = [J]/N$ as well as $[\hat{p}] = [J]/(\text{m}^3/\text{s})$, i.e., the adjoint velocity is dimensionless for this paper's force objectives. For reasons of compactness, the temporal momentum transport is neglected due to the time-averaged perspective and the convective momentum transport is included in the divergence operator of the effective turbulent variables. A variation of the extended cost functional reads

$$L' = J' + \int \hat{v}_i \left[\frac{\partial}{\partial x_k} [v'_k \rho v_i + v_k \rho v'_i + p^{\text{eff}'} \delta_{ik} - 2\mu^{\text{eff}'} S'_{ik}] + \alpha' (v_i - v_i^{\text{tar}}) + \alpha v'_i \right] - \hat{p} \frac{\partial v'_k}{\partial x_k} d\Omega, \quad (9)$$

where a variation of the fluid density and effective turbulent viscosity has been neglected. The latter is usually referred to as frozen-turbulence-assumption and is an delicate assumption, especially for the high Reynolds numbers of this paper, cf. Löhner et al. (2003); Othmer (2008); Stück and Rung (2013); Kröger et al. (2018); Kühl et al. (2021c). However, later applications will show that satisfactory sensitivity derivatives can still be predicted. An isolation of all varied quantities can be developed to

$$L' = \int \bar{p}^{\text{eff}'} n_k r_k - 2\bar{\mu}^{\text{eff}'} \bar{S}'_{ik} n_k r_i d\Gamma^{\text{O}} \quad (10)$$

$$+ \int \hat{v}_i \left[v'_k \rho v_i + v_k \rho v'_i + \bar{p}^{\text{eff}'} \delta_{ik} - \bar{S}'_{ik} 2\bar{\mu}^{\text{eff}'} \right] n_k - \hat{p} v'_k n_k + \bar{\mu}^{\text{eff}'} \frac{\partial \hat{v}_i}{\partial x_k} (v'_i n_k + v'_k n_i) d\Gamma \quad (11)$$

$$+ \int v'_i \left[-\rho v_k \frac{\partial \hat{v}_k}{\partial x_i} - \rho v_k \frac{\partial \hat{v}_i}{\partial x_k} + \frac{\partial}{\partial x_k} [\hat{p} \delta_{ik} - \bar{\mu}^{\text{eff}'} 2\hat{S}_{ik}] + \alpha \hat{v}_i \right] - \bar{p}^{\text{eff}'} \frac{\partial \hat{v}_k}{\partial x_k} \quad (12)$$

$$+ \alpha' \hat{v}_i (v_i - v_i^{\text{tar}}) d\Omega. \quad (13)$$

Striving for $L' = 0$ suggests considering the following system of equations, which eliminates the varied Lagrangian's first volume integral in (12) and is referred to as the the adjoint system of flow equations to the temporally averaged primal Eqns. (1)-(2), viz.

$$-\frac{\partial \hat{v}_k}{\partial x_k} = 0, \quad (14)$$

$$-\rho v_k \frac{\partial \hat{v}_k}{\partial x_i} - \rho v_k \frac{\partial \hat{v}_i}{\partial x_k} + \frac{\partial}{\partial x_k} [\hat{p} \delta_{ik} - \bar{\mu}^{\text{eff}'} 2\hat{S}_{ik}] + \alpha \hat{v}_i = 0. \quad (15)$$

Required boundary conditions can be deduced from remaining boundary integrals (10) - (11), i.e.,

$$\frac{\partial \hat{p}}{\partial n} = 0, \hat{v}_i = -r_i \quad \text{on} \quad \Gamma^{\text{wall}}, \quad (16)$$

$$\frac{\partial \hat{p}}{\partial n} = 0, \hat{v}_i = 0 \quad \text{on} \quad \Gamma^{\text{hor}}, \quad (17)$$

$$\frac{\partial \hat{p}}{\partial n} = 0, \frac{\partial \hat{v}_i}{\partial n} = 0 \quad \text{on} \quad \Gamma^{\text{symm}} \quad (18)$$

$$\hat{p} = 0, \frac{\partial \hat{v}_i}{\partial n} = 0 \quad \text{on} \quad \Gamma^{\text{top}}. \quad (19)$$

More detailed information on the continuous adjoint derivation process can be found, e.g., in Stück (2012); Kröger (2016); Kühl (2021). The remaining contributions to the varied Lagrangian provide access to a local topological sensitivity derivative s , i.e.,

$$L' = \int \alpha' \hat{v}_i (v_i - v_i^{\text{tar}}) d\Omega \quad \xrightarrow{v_i^{\text{tar}}=0} \quad s = \hat{v}_i v_i, \quad (20)$$

based on the inner product between the primal and adjoint velocity vector, cf. Gerdes (2018).

The sensitivity expression indicates the influence of a slight porosity parameter adjustment on the cost function. Various possibilities exist for processing the topological derivative, which usually follows a global or a local optimization method. A prominent representative of the latter refers to the steepest gradient descent method. Therein, a delicate issue refers to the computation of an appropriate porosity gradient field (Gerdes et al. (2014); Vrionis et al. (2021)) that usually contains various physical and technical constraints, such as a never-negative porosity parameter and minimum material thicknesses (De Leon et al. (2015); Alexandersen and Lazarov (2015)). However, once a suitable gradient has been determined, the porosity field is updated by a small porosity update into the direction of steepest descent, and subsequently, the cost functional is re-evaluated based on the new porosity distribution. The outlined process is usually highly automat-able and can generate new shapes of high complexity.

This paper takes a different approach based on a comparatively simple optical screening of the topology sensitivity field’s sign used for improved –but not optimal– material placement. An illustrative example is finding an appropriate container stack position in the direct vicinity of a Flettner rotor.

3 Application

The flow around a Flettner rotor equipped with two end plates is examined in the following. The optimization task refers to an appropriate positioning of six Twenty-foot Equivalent container Units (TEU20). The research question has general character that frequently arises in industrial shipbuilding applications, as Flettner rotors almost always interact with a ship’s superstructure and loading.

The numerical framework employed to approximate the paper’s partial differential equations is based on the segregated primal/dual multiphase flow solver FreSCo^+ , which utilizes a collocated variable storage scheme. This solver adopts an implicit, second-order accurate, segregated Finite-Volume-Method (FVM) operating on unstructured polyhedral meshes that may include hanging nodes (cf. Rung et al. (2009); Stück (2012); Schubert (2019); Manzke (2018)). Primal and adjoint convergence is achieved through a Semi-Implicit Method for Pressure-Linked Equations (SIMPLE), which addresses the pressure–velocity decoupling issue using a momentum-weighted interpolation technique, following the approach of Rhie and Chow (1983); Yakubov et al. (2015); Kühn and Rung (2022). Further information on the employed code can be found, e.g., in Rung et al. (2009); Stück (2012); Manzke (2018); Schubert (2019); Kühn et al. (2021a,b,c). Self-adjoint diffusive fluxes are computed using a second-order Central Difference Scheme (CDS). Primal and adjoint convective fluxes follow a blended approach that combines CDS with the Quadratic Upwind Interpolation for Convective Kinematics (QUICK) method. To balance numerical accuracy and stability while minimizing artificial diffusion, a weighting of 80% CDS and 20% QUICK is applied. A universal wall function, which blends between the viscous sub-layer and a standard wall function Rung et al. (2001); Gritskevich et al. (2017), is employed with a non-dimensional wall adjacent cell height of $y^+ \approx 50$. When combined with a second-order accurate Implicit Three-Time-Level (ITTL) time integration scheme, the resulting numerical method effectively captures turbulence decay, as demonstrated in prior maritime aerodynamic studies Angerbauer and Rung (2020); Pache (2023) using experimental wind tunnel data. The primal/dual approach method has been thoroughly validated; exemplary results are provided in Manzke et al. (2012); Kröger (2016); Angerbauer and Rung (2020) for the primal and in Kröger et al. (2018); Kühn et al. (2021a); Kühn (2024) for the adjoint flow. The numerical strategy is specially tailored for adjoint-based parameter-free shape optimization purposes, cf. Müller et al. (2021); Radtke et al. (2023). Further details on measures that increase the adjoint solver’s numerical stability can be found in Kühn (2025b).

3.1 Stand Alone Consideration

An isolated, full-scale Flettner rotor is examined at $\text{Re}_D = \rho V D / \mu = 2 \cdot 10^6$ or $\text{Re}_H = \rho V H / \mu = 1.2 \cdot 10^7$ and a spinning ratio of $k = \pi D n / V = 3$ based on the fluid properties, the rotor diameter D and height H , and the reference wind speed V at a reference height of $x_{3,\text{ref}} / H = 10/18$. The rotor is mounted at $x_i = [0, 0, 0]^T$, is approached by the flow against the x_1 axis, and rotates around the x_3 axis. The investigation aims to reduce the drag while increasing the lift, represented by $r_i = \delta_{i1}$ and $r_i = \delta_{i2}$ in Eqn. (7) for the drag and lift direction, respectively. Far field boundaries are positioned 100 rotor diameters away from the rotor to minimize the blockage effect. The four horizontal far-field boundaries correspond to velocity boundary conditions, which specify the introduced logarithmic wind profile with a Hellmann exponent of $m = 0.85$. A constant pressure is prescribed at the upper and a symmetry condition is specified at the lower end.

An impression of the corresponding unstructured numerical grid is shown in Fig. 1 (a). Next to the rotor’s vicinity and wake refinement, the wind profile refinement along the horizontal boundaries is indicated. The grid consists of approximately 3.8 million control volumes. Simulations are carried out for 200 equivalent flows around the Flettner rotor, whereby the Courant number is kept below one, resulting in approximately 20 000

time steps of same size. The cumulative averaging starts after 100 equivalent steps. The figure's right part provides an instantaneous impression of the scale-resolving simulation at the simulation's end based on $Q = 100$ iso-lines of the Q-vortex-criterion, where the local vorticity colors the iso-lines. In addition to the smaller vortices in the rotor wake, the tip vortex at the rotor end is particularly recognizable.

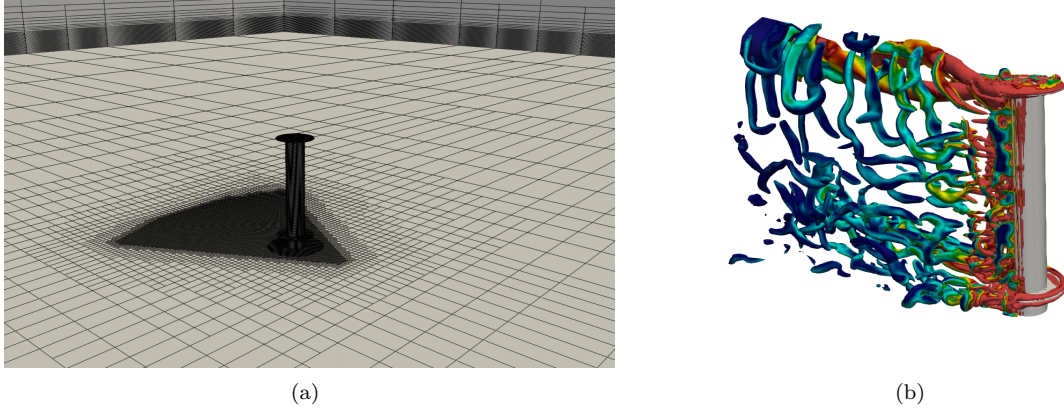


Figure 1: (a) Perspective view of the near-field grid and (b) instantaneous vortex structures colored with the vorticity magnitude of a hybrid averaged/filtered RANS/LES reference simulation at $\text{Re}_H = 1.2 \cdot 10^7$ or $\text{Re}_D = 2 \cdot 10^6$ at $k = 3.0$.

Figure 2 (a) provides impressions of the averaged solution by showing the averaged flow field $|v_i|/V$ on four vertical slices at $x_3/H = [0, 1/3, 2/3, 1]$ together with the pressure coefficient $c_p = (p - P)/(0.5\rho V^2)$ along the rotor. The figure's right part (b) underlines the credibility of the flow prediction by evaluating the ratio of resolved to modeled Turbulent Kinetic Energy (TKE) in the rotor wake. The ratio indicates a resolution of well above 80 percent for the most part, which is typically considered sufficient for scale-resolving flow simulations, cf. Pope (2001); Loft et al. (2023).

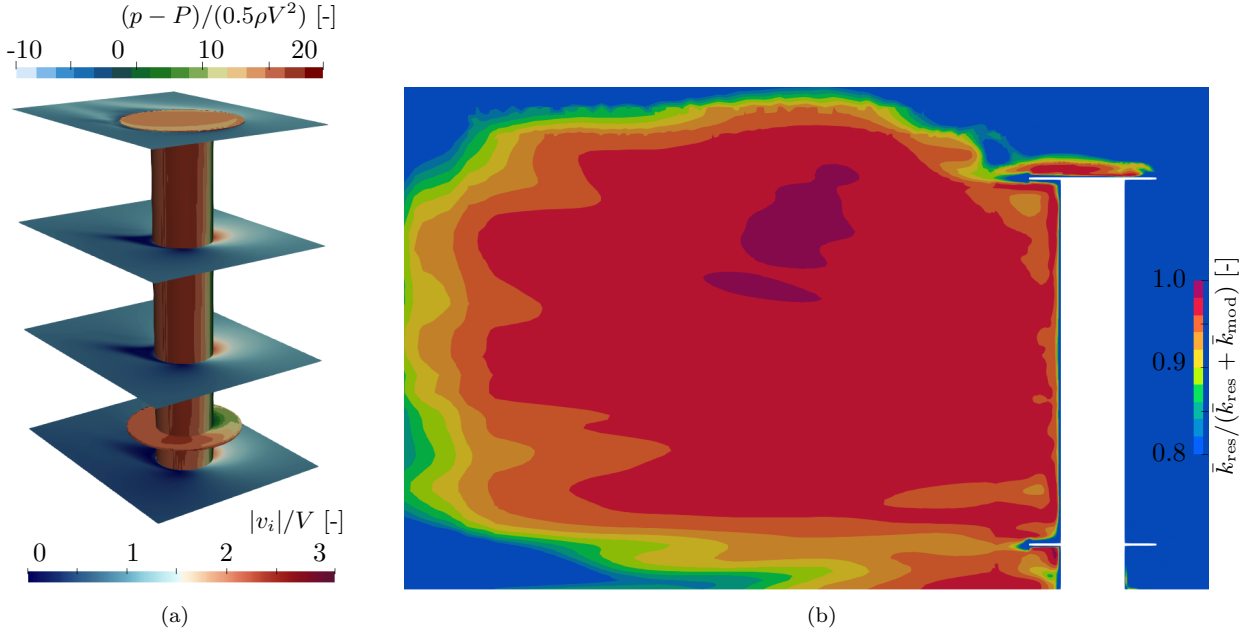


Figure 2: (a) Normalized magnitude of the time-averaged velocity vector $|v_i|/V$ near the rotor on four vertical sectional planes at $x_3/H = [0, 1, 2, 3]/3$ and (b) the ratio of resolved (k_{res}) to total ($k_{\text{res}} + k_{\text{mod}}$) Turbulent Kinetic Energy in the rotor's wake.

3.2 Adjoint Investigation

The temporally converged flow field is passed to the adjoint solver, whereby three different adjoint scenarios are examined, which address (a) the rotor’s drag, (b) its lift, or (c) an equal-part mix referred to as drift, respectively. Since increased lift also increases the induced drag, an alternative investigation could consider the ratio of drag to lift. The necessary adjustment of the adjoint boundary conditions is derived in the App. A. However, in order not to mix the effects, this approach is not pursued. The three adjoint studies differ exclusively in their boundary conditions, see Eqn. (16), which is set to $r_i = \delta_{i1}$, $r_i = \delta_{i2}$, and $r_i = [1, 1]^T/\sqrt{2}$, respectively, for the drag, lift, and drift formulations. The steady adjoint solver converges after about 5000 outer iterations. The resulting dimensionless adjoint velocity fields are shown in Fig. 3 analogously to the presentation of the primal flow from Fig. 2 (a). The horizontal arrangement varies the cost function, with the drag (lift) [drift] results shown on the left (center) [right] and the \hat{v}_1 , \hat{v}_2 , \hat{v}_3 components shown from top to bottom. A greater similarity between the lift and drift than the drag results is recognizable in all three directions.

The product of the averaged primal velocity field from Fig. 2 (a) and the stationary adjoint companion from Fig. 3 provides the topological sensitivity from Eqn. (20). To interpret the sensitivity field in terms of a gradient method, the topological derivative is negated. The result is shown in Fig. 4 for all three cost functional column-wise(cf. Fig. 3) and different horizontal slices at $x_3/H = [0, 1, 2]/3$ row-wise, with blue areas showing negative and yellow areas a positive influence on the respective cost functional. Generally, there appears to be no pronounced vertical gradient in the sensitivity field in all cases, i.e., each column’s sensitivities per cost function are similar. As can already be anticipated from the adjoint velocity fields, the differences between the lift ((b),(e),(h)) and the lift ((c),(f),(i)) functional are relatively small compared to the drag ((a),(d),(g)) functional. Accordingly, the lift and drift function would benefit from starboarded, wind-facing superstructures, where the drift function extends the lift’s positive quadrant slightly in the direction of the resistance function. On the other hand, the drag function accepts the entire starboard area and the region in front of the rotor except for a small spot that sweeps in wind direction out of the rotor.

3.3 Validation

The optically evaluated sensitivity fields are used to check their prediction quality. For this purpose, four situations are examined, all of which position six TEU20 containers (total height of $h_{\text{cont.}}/H = 0.8636$) stacked on top of each other at different positions relative to the rotor. Two studies take up the similar lift and drift sensitivities and place the stack clearly on both the positive (starboard at $[x_1, x_2]/H = [1/5, -1/3]$) and the negative (port at $[x_1, x_2]/H = [1/5, 1/3]$) sides. The drag situation is also examined twice, but in this case, two times in the positively predicted region, in which the container stack is positioned once in front of the rotor ($[x_1, x_2]/H = [1/3, 0]$) and once behind on the starboard side ($[x_1, x_2]/H = [-1/3H, -1/3H]$). The respective arrangements are shown in Fig. 5 from (a) to (c), respectively.

The four scenarios are examined analogously to the stand-alone initial analysis, i.e., a time horizon of 200 equivalent rotor flows is considered, where the averaging process starts after 100 flow cycles. The utilized numerical grids are shown in Fig. 6. The rotor’s discretization is adopted for the container stacks, and the grid size increases to approximately 4.1 million control volumes.

The force results of the additional four investigations are shown in Fig. 7 relative to the initial results via $(J - J_{\text{ref}})/J_{\text{ref}} \cdot 100\%$, with the relative changes in the drag coefficient depicted in blue and the lift in red. The intention of the respective arrangement is validated, i.e., arrangement (a) features an increase, and arrangement (b) a reduced lift coefficient. In contrast, both drag coefficients in arrangements (c) and (d) are reduced, where the arrangement with a rear placed container (c) leads to a less pronounced decrease in lift. Interestingly, the decreases in the drag coefficient are of similar magnitude in both cases around 50 percent. In contrast, the drag coefficient for arrangement (a) increases significantly. Since the lift coefficient increases by approximately twenty percent, the drag increase seems not only to be a matter of parasitic but also of induced drag effects.

4 Conclusion and Outlook

The paper presented a method for determining topological sensitivities for optimization based on a porous flow formulation – without directly considering the porosity field. Instead, an indirect, adjoint method was used to determine the sensitivity with respect to the porosity parameter. Subsequently, the calculated topological sensitivity was not considered in an actual optimization process but instead examined vividly by identifying spatial regions that lead to improved –but not optimal– flow behavior. The proposed method needs no adjustments to existing primal and adjoint flow solvers, e.g., for shape optimization purposes, as the strategy can be interpreted as alternative post-processing, making the proposed method especially attractive in an early design phase.

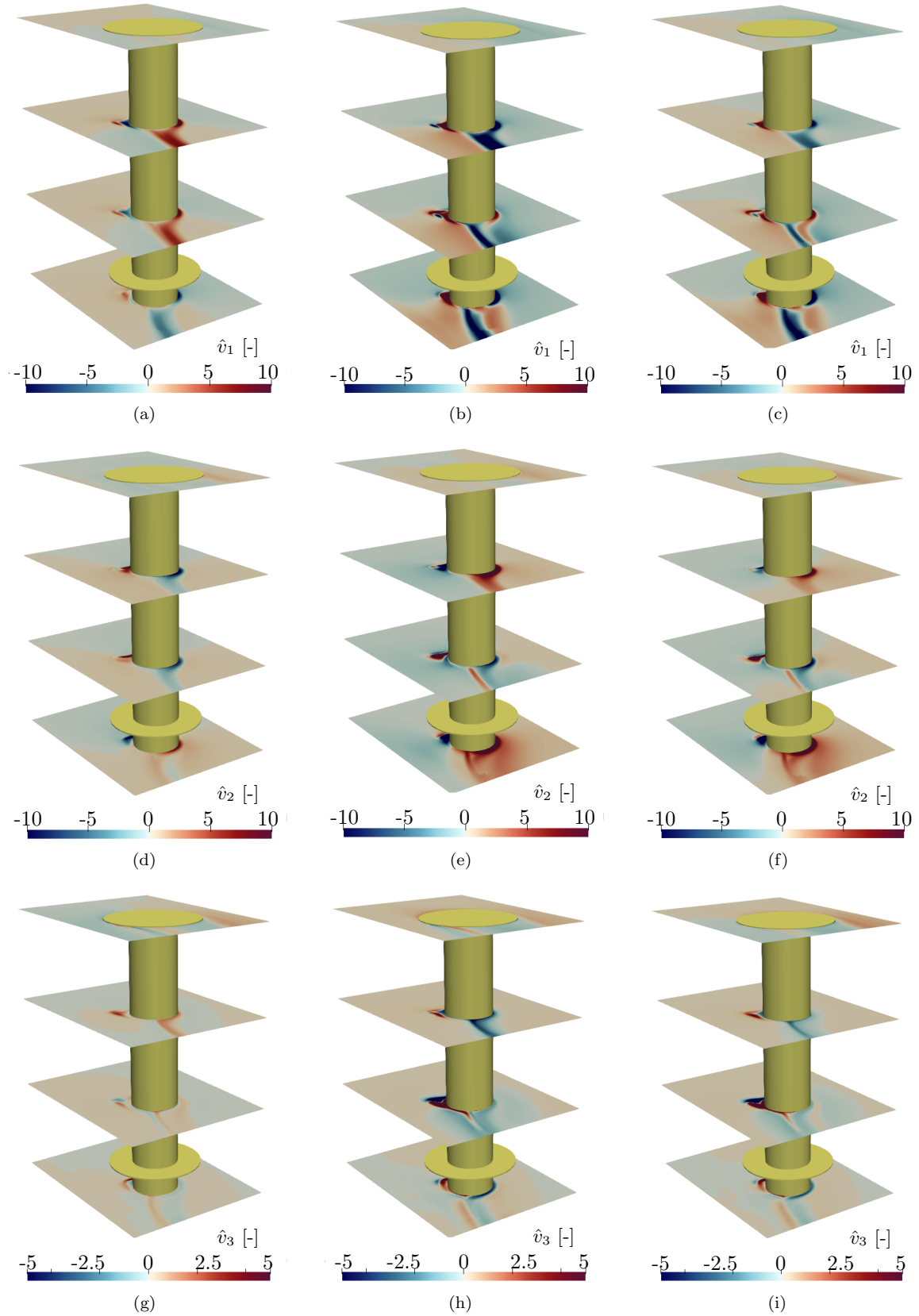


Figure 3: Representation of the adjoint velocity vector components (row-wise) for the three cost functional under consideration (column-wise, i.e., drag: (a),(d),(g); lift: (b),(e),(h); drift: (c),(f),(i)).

The paper's application addressed the time-averaged performance of a Flettner rotor in an idealized wind tunnel employing the frozen-turbulence assumption. Different porosity sensitivity fields have been obtained for

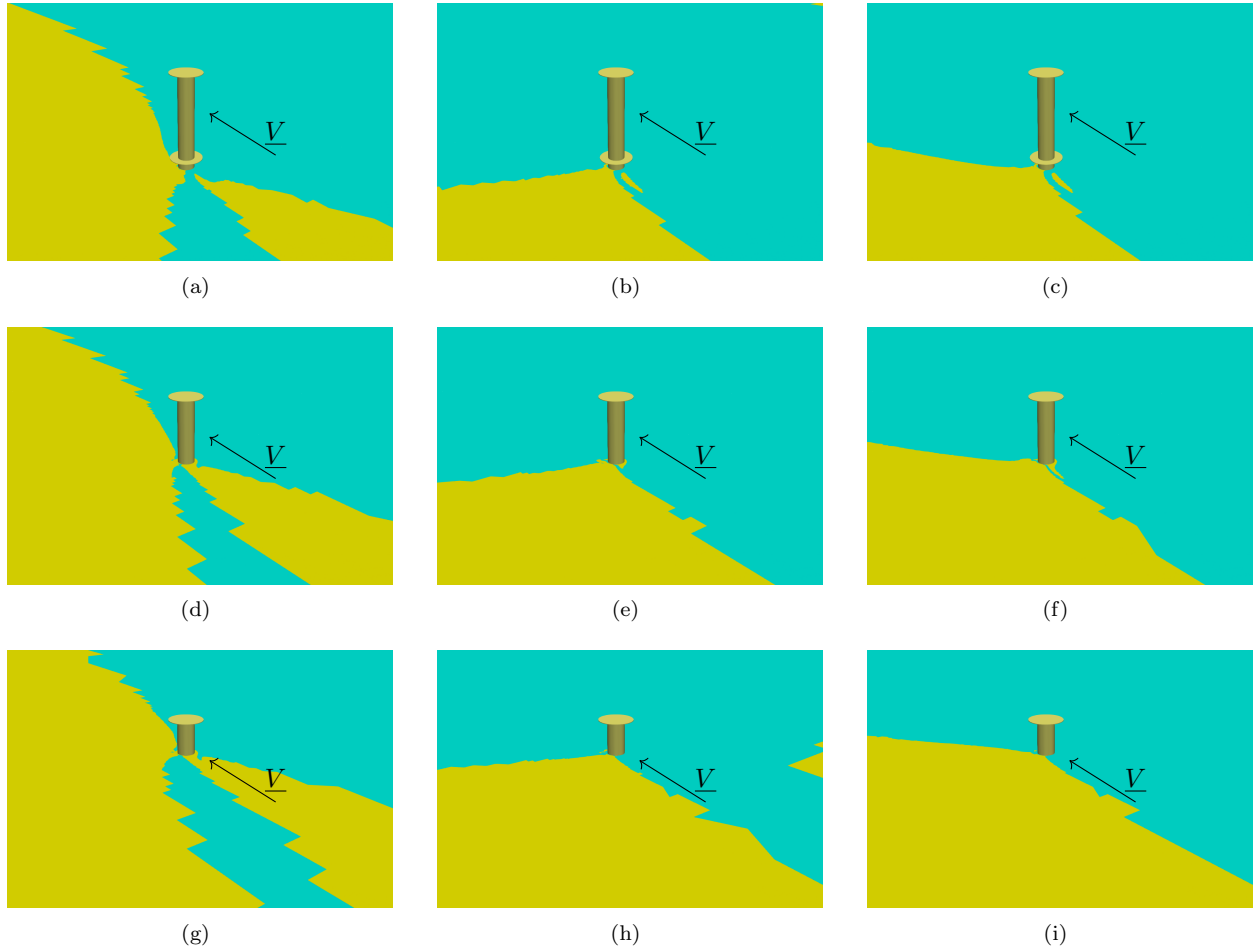


Figure 4: Topological sensitivity along three sections at different vertical positions (row-wise) and for three different cost functional (column-wise). Blue areas indicate a negative, and yellow areas a positive impact on the respective function.

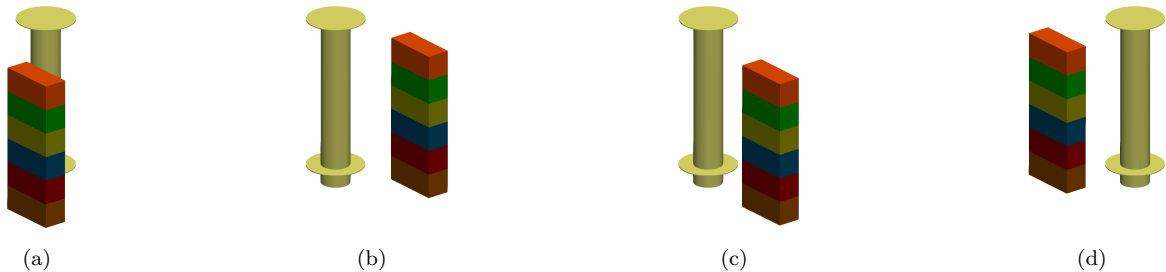


Figure 5: Four different container-rotor arrangements, where the first two (a)-(b) are used to examine the lift/drift functional and the lower two (c)-(d) are used to examine the drag functional.

diverse force-cost functional, such as rotor drag and lift. The prediction quality was checked and validated by placing a container stack in cost-functional improving or deteriorating areas.

In the future, well-founded validation studies could be carried out using alternative methods to determine the topological sensitivity, such as linearized simulation approaches or Finite-Difference-Methods. Furthermore, the necessity of the correct differentiation of the flow turbulence model should be considered.

The strategy can also be used for related questions, such as design proposals for hydrodynamic propulsion-improving devices in aft ship or aerodynamic windshields in for ship regions. Since only the sign of the topological sensitivity was checked in this paper, future investigations should strive for authentic, local topology optimizations, utilizing, e.g., a gradient descent method by actually considering the porosity field. Furthermore, a central topic should be implementing the presented method into a holistic and robust design investigation considering

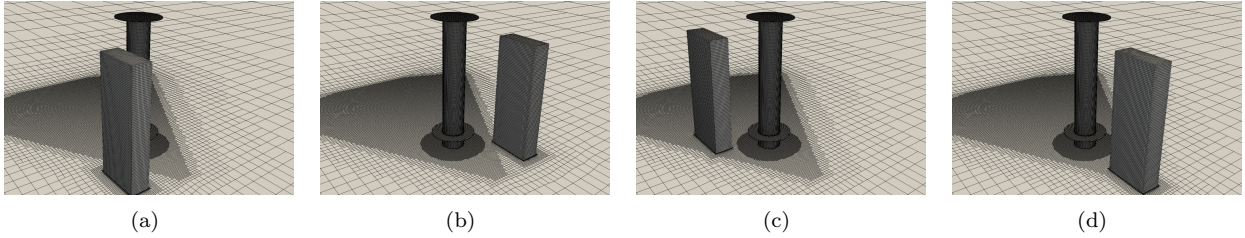


Figure 6: Numerical grids for the four different container-rotor arrangements from Fig. 5.

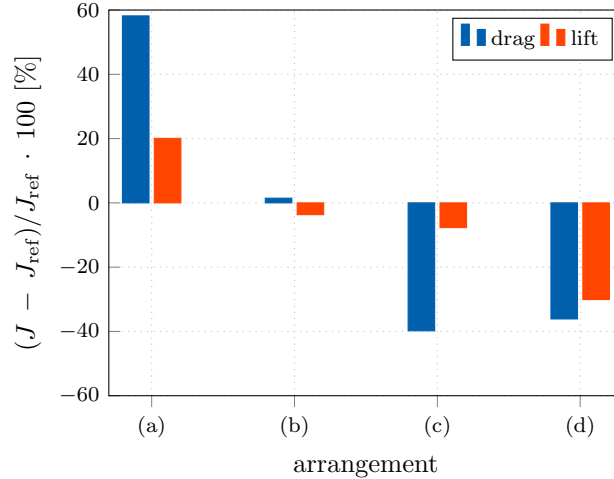


Figure 7: Relative changes in the lift and drag cost functions for the arrangements considered in Fig. 5.

different operating conditions such as wind speeds and apparent wind angles.

5 Declaration of Competing Interest

The author declares that he has no known competing financial interests or personal relationships that could have appeared to influence the work reported in this paper.

6 Acknowledgments

The current work is part of the “Propulsion Optimization of Ships and Appendages” (Grant No. 03SX599C) and “Development of a Comprehensive Methodology for the Integration of Flettner Rotors on Different Ship Types” (Grant No. 03SX581G) research projects funded by the German Federal Ministry for Economics and Climate Action. The author gratefully acknowledges this support.

References

- J. Alexandersen and B.S. Lazarov. Topology Optimisation of Manufacturable Microstructural Details Without Length Scale Separation Using a Spectral Coarse Basis Preconditioner. *Computer Methods in Applied Mechanics and Engineering*, 290:156–182, 2015. doi:10.1016/j.cma.2015.02.028.
- R. Angerbauer and T. Rung. Hybrid RANS/LES Simulations of Aerodynamic Flows Around Superstructures of Ships. In *17th Symposium on Hybrid RANS-LES Methods*, 17–19 September, 2018, Berlin, Germany, pages 367–377. Springer, 2020. doi:10.1007/978-3-030-27607-2_30.
- M.P. Bendsoe and O. Sigmund. *Topology Optimization: Theory, Methods, and Applications*. Springer Science & Business Media, 2013.

- L. Blank, H. Garcke, L. Sarbu, T. Srisupattarawanit, V. Styles, and A. Voigt. Phase-Field Approaches to Structural Topology Optimization. Constrained Optimization and Optimal Control for Partial Differential Equations, pages 245–256, 2012. doi:10.1007/978-3-0348-0133-1_13.
- T. Borrvall and J. Petersson. Topology Optimization of Fluids in Stokes Flow. International Journal for Numerical Methods in Fluids, 41(1):77–107, 2003. doi:10.1002/fld.426.
- D.M. De Leon, J. Alexandersen, J.S. O. Fonseca, and O. Sigmund. Stress-Constrained Topology Optimization for Compliant Mechanism Design. Structural and Multidisciplinary Optimization, 52:929–943, 2015. doi:10.1007/s00158-015-1279-z.
- H. Garcke, C. Hecht, M. Hinze, and C. Kahle. Numerical Approximation of Phase Field Based Shape and Topology Optimization for Fluids. SIAM Journal on Scientific Computing, 37(4):A1846–A1871, 2015. doi:10.1137/140969269.
- N.R. Gauger, A. Walther, C. Moldenhauer, and M. Widhalm. Automatic Differentiation of an Entire Design Chain for Aerodynamic Shape Optimization. In New Results in Numerical and Experimental Fluid Mechanics VI, pages 454–461. Springer, 2008. doi:10.1007/978-3-540-74460-3_56.
- A. Gerdes. Fluid Dynamic Optimization of HVAC-Components with Adjoint Methods. PhD thesis, Hamburg University of Technology, 2018.
- A. Gerdes, M. Hinze, and T. Rung. An Efficient Line Search Technique and Its Application to Adjoint Topology Optimisation. PAMM, 14(1):719–720, 2014. doi:10.1002/pamm.201410342.
- A. Gersborg-Hansen, O. Sigmund, and R. B. Haber. Topology Optimization of Channel Flow Problems. Structural and Multidisciplinary Optimization, 30(3):181–192, 2005. doi:10.1007/s00158-004-0508-7.
- M.B. Giles and N.A. Pierce. Adjoint Equations in CFD: Duality, Boundary Conditions and Solution Behaviour. AIAA Paper, 1997. doi:10.2514/6.1997-1850. AIAA–97–1850.
- M.B. Giles and N.A. Pierce. An Introduction to the Adjoint Approach to Design. Flow, Turbulence and Combustion, 65(3):393–415, 2000. doi:10.1023/A:1011430410075.
- M.S. Gritskevich, A.V. Garbaruk, J. Schütze, and F.R. Menter. Development of DDES and IDDES Formulations for the $k-\omega$ Shear Stress Transport Model. Flow, Turbulence and Combustion, 88(3):431–449, 2012. doi:10.1007/s10494-011-9378-4.
- M.S. Gritskevich, A.V. Garbaruk, and F.R. Menter. A Comprehensive Study of Improved Delayed Detached Eddy Simulation with Wall Functions. Flow, Turbulence and Combustion, 98:461–479, 2017. doi:10.1007/s10494-016-9761-2.
- J.K. Guest and J.H. Prévost. Topology Optimization of Creeping Fluid Flows using a Darcy-Stokes Finite Element. International Journal for Numerical Methods in Engineering, 66(3):461–484, 2006. doi:10.1002/nme.1560.
- F. Klemens, B. Förster, M. Dorn, G. Thäter, and M.J. Krause. Solving Fluid Flow Domain Identification Problems with Adjoint Lattice Boltzmann Methods. Computers & Mathematics with Applications, 79(1):17–33, 2020. doi:10.1016/j.camwa.2018.07.010.
- J. Kröger. A Numerical Process for the Hydrodynamic Optimisation of Ships. PhD thesis, Hamburg University of Technology, 2016.
- J. Kröger, N. Kühn, and T. Rung. Adjoint Volume-of-Fluid Approaches for the Hydrodynamic Optimisation of Ships. Ship Technology Research, 65(1):47–68, January 2018. doi:10.1080/09377255.2017.1411001.
- N. Kühn. Adjoint-Based Shape Optimization Constraint by Turbulent Two-Phase Navier-Stokes Systems. PhD thesis, Hamburg University of Technology, 2021.
- N. Kühn. On the Continuous Adjoint of Prominent Explicit Local Eddy Viscosity-based Large Eddy Simulation Approaches for Incompressible Flows. Flow, Turbulence and Combustion, 113(2):293–330, 2024. doi:10.1007/s10494-024-00543-5.
- N. Kühn. Differential Equation Based Wall Distance Approaches for Maritime Engineering Flows. arXiv preprint arXiv:2504.07286, 2025a.

- N. Kühn. Elliptic Relaxation Strategies to Support Numerical Stability of Segregated Continuous Adjoint Flow Solvers. arXiv preprint arXiv:2501.12518, 2025b.
- N. Kühn and T. Rung. Discrete Adjoint Momentum-Weighted Interpolation Strategies. Journal of Computational Physics, 467:111474, 2022. doi:10.1016/j.jcp.2022.111474.
- N. Kühn, J. Kröger, M. Siebenborn, M. Hinze, and T. Rung. Adjoint Complement to the Volume-of-Fluid Method for Immiscible Flows. Journal of Computational Physics, 440:110411, 2021a. doi:10.1016/j.jcp.2021.110411.
- N. Kühn, P. M. Müller, and T. Rung. Adjoint Complement to the Universal Momentum Law of the Wall. Flow, Turbulence and Combustion, 2021b. doi:10.1007/s10494-021-00286-7.
- N. Kühn, P.M. Müller, and T. Rung. Continuous Adjoint Complement to the Blasius Equation. Physics of Fluids, 33(3):033608, 2021c. doi:10.1063/5.0037779.
- N. Kühn, H. Fischer, M. Hinze, and T. Rung. An Incremental Singular Value Decomposition Approach for Large-Scale Spatially Parallel & Distributed but Temporally Serial Data – Applied to Technical Flows. Computer Physics Communications, 296:109022, 2024. doi:10.1016/j.cpc.2023.109022.
- M. Loft, N. Kühn, M.P. Buckley, J.R. Carpenter, M. Hinze, F. Veron, and T. Rung. Two-phase Flow Simulations of Surface Waves in Wind-Forced Conditions. Physics of Fluids, 35(7), 2023. doi:10.1063/5.0156963.
- R. Löhner, O. Soto, and C. Yang. An adjoint-based design methodology for cfd optimization problems. In 41st Aerospace Sciences Meeting and Exhibit, Reno, Nevada, page 299, 2003. doi:10.2514/6.2003-299.
- M. Manzke. Development of a Scalable Method for the Efficient Simulation of Flows using Dynamic Goal-Orientated Local Grid-Adaption. PhD thesis, Hamburg University of Technology, 2018.
- M. Manzke, J.P. Voss, and T. Rung. Sub-Cycling Strategies for Maritime Two-Phase Flows. In Notes on Numerical Fluid Mechanics and Multidisciplinary Design, volume 120, pages 237–251. Springer, 2012. doi:10.1007/978-3-642-33221-0_14.
- P. M. Müller, N. Kühn, M. Siebenborn, K. Deckelnick, M. Hinze, and T. Rung. A Novel p -Harmonic Descent Approach Applied to Fluid Dynamic Shape Optimization. Structural and Multidisciplinary Optimization, 2021. doi:10.1007/s00158-021-03030-x.
- S. K. Nadarajah. The Discrete Adjoint Approach to Aerodynamic Shape Optimization. PhD thesis, Stanford University, 2003.
- S. Nørgaard, O. Sigmund, and B. Lazarov. Topology Optimization of Unsteady Flow Problems Using the Lattice Boltzmann Method. Journal of Computational Physics, 307:291–307, 2016. doi:10.1016/j.jcp.2015.12.023.
- L.H. Olesen, F. Okkels, and H. Bruus. A High-Level Programming-Language Implementation of Topology Optimization Applied to Steady-State Navier–Stokes Flow. International Journal for Numerical Methods in Engineering, 65(7):975–1001, 2006. doi:10.1002/nme.1468.
- C. Othmer. A Continuous Adjoint Formulation for the Computation of Topological and Surface Sensitivities of Ducted Flows. International Journal for Numerical Methods in Fluids, 58(8):861–877, 2008. doi:10.1002/fld.1770.
- C. Othmer, D.E. Manosalvas-Kjono, A. Jameson, and J.J. Alonso. Aerodynamic Topology Optimization: Some Observations on Hysteresis in Separated Flows. In 23rd AIAA Computational Fluid Dynamics Conference, page 4413, 2017. doi:10.2514/6.2017-4413.
- R. Pache. Datenbasierte Modellierung der Aerodynamischen Lasten auf Überwasserschiffe. PhD thesis, Hamburg University of Technology, 2023.
- E.M. Papoutsis-Kiachagias and K.C. Giannakoglou. Continuous Adjoint Methods for Turbulent Flows, Applied to Shape and Topology Optimization: Industrial Applications. Archives of Computational Methods in Engineering, 23(2):255, 2016. doi:10.1007/s11831-014-9141-9.
- A. Pizzolato, A. Sharma, K. Maute, A. Sciacovelli, and V. Verda. Topology Optimization for Heat Transfer Enhancement in Latent Heat Thermal Energy Storage. International Journal of Heat and Mass Transfer, 113:875–888, 2017. doi:10.1016/j.ijheatmasstransfer.2017.05.098.

- A. Pizzolato, A. Sharma, K. Maute, A. Sciacovelli, and V. Verda. Multi-Scale Topology Optimization of Multi-Material Structures with Controllable Geometric Complexity – Applications to Heat Transfer Problems. Computer Methods in Applied Mechanics and Engineering, 357:112552, 2019. doi:10.1016/j.cma.2019.07.021.
- S.B. Pope. Turbulent Flows. Cambridge University Press, 2001.
- L. Radtke, G. Bletsos, N. Kühl, T. Suchan, T. Rung, A. Düster, and K. Welker. Parameter-Free Shape Optimization: Various Shape Updates for Engineering Applications. Aerospace, 10(9), 2023. doi:10.3390/aerospace10090751.
- C.M. Rhie and W. L. Chow. Numerical Study of the Turbulent Flow Past an Airfoil with Trailing Edge Separation. AIAA Journal, 21(11):1525–1532, 1983. doi:10.2514/3.8284.
- R. Roth and S. Ulbrich. A Discrete Adjoint Approach for the Optimization of Unsteady Turbulent Flows. Flow, Turbulence and Combustion, 90:763–783, 2013. doi:10.1007/s10494-012-9439-3.
- E. Ruberto. An Adjoint Based Topology Optimization for Flows Including Heat Transfer. PhD thesis, Politecnico di Milano, 2016.
- T. Rung, H.M. Lübcke, and F. Thiele. Universal Wall-Boundary Conditions for Turbulence Transport Models. Journal of Applied Mathematics and Mechanics, 81:481–482, 2001. doi:10.1002/zamm.20010811520.
- T. Rung, K. Wöckner, M. Manzke, J. Brunswig, C. Ulrich, and A. Stück. Challenges and Perspectives for Maritime CFD Applications. Jahrbuch der Schiffbautechnischen Gesellschaft, 103:127–39, 2009.
- S. Schubert. Analysis of Coupling Techniques for Overset-Grid Finite-Volume Methods. PhD thesis, Hamburg University of Technology, 2019.
- J. Seifert. A review of the Magnus Effect in Aeronautics. Progress in Aerospace Sciences, 55:17–45, 2012. doi:10.1016/j.paerosci.2012.07.001.
- O. Sigmund and K. Maute. Topology optimization approaches: A comparative review. Structural and Multidisciplinary Optimization, 48(6):1031–1055, 2013. doi:10.1007/s00158-013-0978-6.
- A. Stück. Adjoint Navier-Stokes Methods for Hydrodynamic Shape Optimisation. PhD thesis, Hamburg University of Technology, 2012.
- A. Stück and T. Rung. Adjoint Complement to Viscous Finite-Volume Pressure-Correction Methods. Journal of Computational Physics, 248:402–419, 2013. doi:10.1016/j.jcp.2013.01.002.
- P.Y. Vrionis, K.D. Samouchos, and K.C. Giannakoglou. Topology Optimization in Fluid Mechanics Using Continuous Adjoint and the Cut-Cell Method. Computers & Mathematics with Applications, 97:286–297, 2021. doi:10.1016/j.camwa.2021.06.002.
- K. Woeckner, W. Drazyk, and T. Rung. An Efficient VoF-based RANS Method to Capture Complex Sea States. In International Conference on Offshore Mechanics and Arctic Engineering, volume 49149, pages 755–763, 2010.
- S. Xu, W. Jahn, and J.D. Müller. CAD-Based Shape Optimisation with CFD Using a Discrete Adjoint. International Journal for Numerical Methods in Fluids, 74(3):153–168, 2014. doi:10.1002/flid.3844.
- S. Yakubov, T. Maquil, and T. Rung. Experience Using Pressure-Based CFD Methods for Euler-Euler Simulations of Cavitating Flows. Computers & Fluids, 111:91–104, 2015. doi:10.1016/j.compfluid.2015.01.008.
- G. Yu, J.D. Müller, D. Jones, and F. Christakopoulos. CAD-Based Shape Optimisation Using Adjoint Sensitivities. Computers & Fluids, 46(1):512–516, 2011. doi:10.1016/j.compfluid.2011.01.043.

A Adjoint Boundary Conditions for Drag-To-Lift-Ratio Cost Functional

Considering the following, alternative cost functional that relates the paper's rotor drag ($r_i = \delta_{i1}$) and lift ($r_i = \delta_{i2}$) by rewriting Eqn. (7) to

$$J = \frac{D}{L} = \frac{\int [\bar{p}^{\text{eff}} \delta_{ik} - 2\bar{\mu}^{\text{eff}} \bar{S}_{ik}] n_k \delta_{i2} d\Gamma^{\text{O}}}{\int [\bar{p}^{\text{eff}} \delta_{ik} - 2\bar{\mu}^{\text{eff}} \bar{S}_{ik}] n_k \delta_{i2} d\Gamma^{\text{O}}}. \quad (21)$$

A linearization yields

$$J' = \frac{1}{L} D' - \frac{D}{L^2} L' \quad \text{with} \quad D' = \int [\bar{p}^{\text{eff}} \delta_{ik} - 2\bar{\mu}^{\text{eff}} \bar{S}_{ik}]' n_k \delta_{i1} d\Gamma^{\text{O}} \quad (22)$$

$$\text{and} \quad L' = \int [\bar{p}^{\text{eff}} \delta_{ik} - 2\bar{\mu}^{\text{eff}} \bar{S}_{ik}]' n_k \delta_{i2} d\Gamma^{\text{O}}, \quad (23)$$

that can be combined to

$$J' = \int [\bar{p}^{\text{eff}} \delta_{ik} - 2\bar{\mu}^{\text{eff}} \bar{S}_{ik}]' n_k \left[\frac{1}{L} \delta_{i1} - \frac{D}{L^2} \delta_{i2} \right] d\Gamma^{\text{O}}, \quad (24)$$

resulting in modified boundary conditions for the adjoint velocity field along the rotor, i.e., substitute $\hat{v}_i = \frac{D}{L^2} \delta_{i2} - \frac{1}{L} \delta_{i1}$ in Eqn. (16).